Highlights

Nighttime convection in water-ice clouds at high northern latitudes on Mars

David Hinson,Huiqun Wang,John Wilson,Aymeric Spiga

- We analyzed temperature profiles and wide-angle images from Mars Global Surveyor.
- Radio occultation profiles resolve km-scale features associated with water-ice clouds.
- Convective mixing occurs at night within water-ice clouds at high northern latitudes.
- There is widespread nocturnal convection within the summer-season annular cloud.
- The spatial structure of the annular cloud varies strongly with time of day.

Nighttime convection in water-ice clouds at high northern latitudes on Mars

David Hinson[a,*], Huiqun Wang[b], John Wilson[c] and Aymeric Spiga[d]

[a]Carl Sagan Center, SETI Institute, Mountain View, CA 94043, USA
[b]Smithsonian Astrophysical Observatory, Harvard-Smithsonian Center for Astrophysics, Cambridge, MA 02138, USA
[c]Space Science and Astrobiology Division, NASA Ames Research Center, Moffett Field, CA 94035, USA
[d]Sorbonne Université / Laboratoire de Météorologie Dynamique, 4 Place Jussieu, 75252 Paris, France

ARTICLE INFO

Keywords:
Mars
Atmospheres, dynamics
Meteorology

ABSTRACT

We investigate water-ice clouds and their influence on the temperature structure of the Martian atmosphere at high northern latitudes in early summer. New results are obtained through coordinated analysis of two types of data from Mars Global Surveyor: atmospheric profiles retrieved from radio occultation (RO) measurements and wide-angle images from the Mars Orbiter Camera (MOC). Some RO profiles contain a layer of neutral static stability, which indicates the presence of convective mixing at a local time (about 5 h) when it does not usually occur. These nocturnal mixed layers (NMLs) were observed frequently in early summer of Mars year 27 at latitudes of 53–72°N and longitudes of 210–330°E. The base of a typical NML is 3 km above the surface, about the same height as the nighttime cloud layer detected by the Phoenix LIDAR in early summer of Mars year 29 at 234°E, 68°N. The depth of the NMLs ranges from less than 1 km to more than 5 km. Comparisons with nearly simultaneous MOC images demonstrate that NMLs are closely associated with water-ice clouds. There is a dense cluster of NMLs within the annular cloud that appears every year in early summer between Alba Mons and the north polar residual ice cap. The lighting conditions at this location and season allowed MOC to observe the annular cloud on most orbits, at 118-min intervals. Its appearance varies dramatically with local time, becoming more symmetrical and better organized at night and dissipating to a crescent shape during the day. According to high-resolution numerical simulations (Spiga et al., 2017), including a large-eddy simulation at the Phoenix landing site, NMLs form when radiative cooling by water-ice aerosols causes convective instability; the mixed layer is forced from above by negative buoyancy. Our results strongly support this conclusion. In addition, MOC images from midsummer contain eastward-moving frontal clouds. Temperature profiles within these clouds show signs of near-surface advection of warm air, which reduces the static stability of the lower atmosphere and contributes, along with cloud radiation, to the formation of an NML.

1. Introduction

Water-ice clouds strongly influence air temperatures on Mars through their effect on radiative transfer. They emit infrared radiation, and they absorb infrared radiation emitted by the surface as well as a small amount of sunlight. The net result is cloud-level heating during the day, when the surface is hot and the clouds are exposed to sunlight, and cloud-level cooling at night, when the surface is cold and sunlight is absent (Wilson et al., 2008; Madeleine et al., 2012). In addition, the infrared radiation emitted by the clouds can significantly warm the surface at night (Wilson et al., 2007; Wilson and Guzewich, 2014). At low latitudes, water-ice clouds are most common and their impact on air and surface temperatures is largest in late spring and early summer of the northern hemisphere (the aphelion season), when the column abundance of water vapor is relatively large and the atmosphere is cool (Smith, 2004).

Radiative cooling by water-ice clouds has important consequences for the structure and dynamics of the lower atmosphere. Numerical simulations have shown that the nighttime cooling rate is sufficient to generate a substantial temperature inversion (Haberle et al., 1999; Colaprete and Toon, 2000). This type of inversion has been observed at local times a few hours before sunrise in the tropics, where the aphelion-season clouds interact with the thermal tides (Hinson and Wilson, 2004; Wilson and Guzewich, 2014). Adiabatic heating and cooling by the tides affects the spatial

*Corresponding author
dhinson@seti.org (D. Hinson); hwang@cfa.harvard.edu (H. Wang); robert.j.wilson@nasa.gov (J. Wilson); aymeric.spiga@lmd.ipsl.fr (A. Spiga)
ORCID(s): 0000-0002-1620-4011 (D. Hinson)

distribution of the clouds and its evolution with time of day. The radiative cooling by the clouds is therefore correlated with the temperature field of the tides, enabling cloud radiation to strengthen the tides. This tide-cloud interaction results in nighttime inversions as large as 20–30 K in the Tharsis region (Hinson and Wilson, 2004).

The impact of water-ice clouds extends beyond the nighttime temperature inversions. Predawn radio occultation (RO) profiles from the tropics contain unexpected layers of neutral stability at a height of about 5–10 km above the ground (Hinson et al., 2014). They appear primarily in Arabia Terra and the Tharsis region, where the surface elevation is relatively high (Hinson et al., 2018). This type of nocturnal mixed layer (NML) forms when radiative cooling in a water-ice cloud layer triggers convective instability, as proposed by Hinson et al. (2014) and demonstrated through high-resolution numerical simulations by Spiga et al. (2017). Cloud-induced convection dramatically changes a region of the lower atmosphere previously thought to be stably stratified and relatively calm at night. According to a large-eddy simulation (LES), which resolves sub-km-scale convective motion, vertical wind speeds can reach ± 10 m s^{-1} at night within the 8-km-deep mixed layer adjacent to Arsia Mons (Spiga et al., 2017). To put this into context, the NML is as deep as the daytime convective boundary layer in the Tharsis region (Hinson et al., 2019) and the eddy mixing at night is no less vigorous than in the day (Spiga et al., 2010a,b). The NML and the cloud in which it forms dissipate after sunrise in response to adiabatic heating by the tides, enhanced emission of infrared radiation by the surface, and the daytime increase in air temperature in the boundary layer.

In this paper we use a combination of RO profiles from Mars Global Surveyor (MGS) and wide-angle images from the MGS Mars Orbiter Camera (MOC) to investigate water-ice clouds at high northern latitudes in the summer season. We present new results concerning the spatial structure of the polar clouds, their variation with time of day, and the NMLs that form in response to cloud emission of infrared radiation. This is the first time NMLs have been observed outside the tropics and the most thorough characterization of NMLs to date. Most of the RO profiles with NMLs are from local times (4-6 h) when the Sun is roughly 10° above the horizon, so that nearly simultaneous, collocated MOC images are available. The images show that several types of polar clouds give rise to NMLs.

We supplement the MGS data with observations by the Mars Climate Sounder (MCS) onboard Mars Reconnaissance Orbiter (Kleinböhl et al., 2009; McCleese et al., 2010). MCS measures both air and surface temperatures at two local times, providing context for understanding the diurnal cycle of the polar clouds. The MCS results are discussed at the end of Section 4.3.

Every year in early northern summer, a distinctive annular cloud appears directly north of Alba Mons[1] in Vastitas Borealis. It signals the presence of a polar cyclone with a diameter of more than 1000 km. The annular cloud has been observed for more than 10 consecutive Mars years, first by the Hubble Space Telescope and then by cameras on MGS, Mars Express, and Mars Reconnaissance Orbiter (Sánchez-Lavega et al., 2018, Table 2). Some aspects of cloud morphology are the same in all years, such as the presence of a cloud-free core whose size changes with time of day, but there is significant year-to-year variability, most notably the presence of a double cyclone in some years and a single cyclone in others (Sánchez-Lavega et al., 2018). As we show in Section 4, the annular cloud is responsible for most of the NMLs described in this paper; MOC monitored the spatial structure and diurnal evolution of the cloud while the RO profiles recorded its effect on the temperature and static stability of the atmosphere.

Tyler and Barnes (2014) used a mesoscale model to investigate the circulation and dynamics of the polar atmosphere at the season of the annular cloud. The simulation generates a cyclonic disturbance at the right location, north of Alba Mons, and its 10 m s^{-1} winds are consistent with the 5-20 m s^{-1} tangential velocities derived by tracking features in spacecraft images (Sánchez-Lavega et al., 2018). More generally, the model demonstrates that the annular cloud forms within a complex and rapidly evolving circulation characterized by strong slope flows, a western boundary current, and a large-scale topographically driven thermal circulation.

The detached water-ice cloud layer detected by the Phoenix LIDAR in Vastitas Borealis is the western edge of the annular cloud. From early summer onward, the cloud layer formed at night roughly 2–5 km above the landing site (234°E, 68°N) and then dissipated during the day (Whiteway et al., 2009; Dickinson et al., 2010). (See Sánchez-Lavega et al. (2018) for the view from orbit during the Phoenix mission.) Spiga et al. (2017) conducted an LES (like the one near Arsia Mons) to explore the radiative and dynamical effects of this cloud. The model predicts that nighttime radiative cooling by the water-ice aerosols is sufficient to cause convective instability and the formation of a 2.5-km-deep mixed layer. Our results strongly support this conclusion—most RO profiles from within the annular cloud contain an NML, including some in the vicinity of the Phoenix landing site.

Before proceeding, it is useful to review the conventions for timekeeping on Mars. The term "sol" denotes the

[1] A note on terminology: Alba Patera refers only to the caldera at the summit of the Alba Mons volcano.

mean solar day of 88,775 s. Local time is expressed in true solar hours (24 per sol). Seasons are defined by L_s, the angular position of Mars in its orbit about the Sun, with $L_s \equiv 0°$ at the vernal equinox of the northern hemisphere. As proposed by Clancy et al. (2000), 11 April 1955 is designated as the start of Mars year 1 (MY1). For further discussion of timekeeping on Mars, see Allison (1997) and Allison and McEwen (2000).

The paper is organized as follows. Section 2 introduces the data used in this investigation. Section 3 explains our method for identifying NMLs in RO profiles. The results appear in Section 4, which describes the distribution of the NMLs in season, latitude, and longitude; their association with polar clouds observed from orbit; and the diurnal cycle of the annular cloud. Section 5 reviews and interprets the results. Appendix A provides access to supplementary data.

2. MGS data

MGS circled Mars in a sun-synchronous polar orbit, crossing the equator at local times of about 2 and 14 h and traveling from south to north on the dayside. The orbit period was about 118 min, so that the ground track moved westward by about 29° per orbit. This investigation is based on atmospheric profiles retrieved from RO measurements and images acquired by the MOC wide-angle cameras.

2.1. Radio occultation profiles

MGS performed RO experiments with a 3.6-cm wavelength signal transmitted by the spacecraft and received by a tracking station of the NASA Deep Space Network (DSN). Hinson et al. (1999) describe the procedure used to retrieve atmospheric profiles. The fundamental result from each experiment is a profile of refractive index μ versus planetocentric radius r. Profiles of temperature $T(r)$, pressure $p(r)$, and potential temperature $\theta(r)$ are derived from $\mu(r)$ using independent measurements of the atmospheric composition, which cannot be determined from the RO data. All profiles shown in this paper are for a "dry" atmosphere composed of CO_2, N_2, and ^{40}Ar with relative abundances as measured by the Viking Landers (Owen, 1992). Neglect of water vapor causes a small bias in the retrieved profiles, as discussed in Section 3.

The base of a typical RO profile is 500 m above ground level (AGL), the top is at the 10-Pa pressure level (40 km), and the sample spacing is 700 m. The 1-σ uncertainties in T and p vary strongly with pressure, decreasing from 7% at the top of the profile to 1.2% at 100 Pa and 0.3% near the surface. The uncertainty in radius is only a few meters, commensurate with the accuracy of the MGS orbit reconstructions (Lemoine et al., 2001).

The vertical resolution of the RO profiles is diffraction limited to about 500 m (Karayel and Hinson, 1997). The horizontal resolution along the line of sight from spacecraft to Earth can be estimated as follows. A radio signal traveling through the atmosphere of Mars traverses a layer of depth d in a distance $L \approx 2\sqrt{2\,r_m\,d}$, where r_m is the radius of Mars. The value of d appropriate to this investigation is about 5 km, the characteristic vertical scale of cloud-related structure in the RO profiles. The corresponding value of L is 360 km, or about a 6° arc of a great circle.

RO measurements can be performed only at a sequence of locations determined by the spacecraft orbit, the direction from spacecraft to Earth, and the orientations of the pole vector and prime meridian of Mars at the time of each observation. The objectives of this investigation require profiles at high latitudes in the northern hemisphere during the spring and summer seasons, which were acquired in MY25–27. Section 4.1 describes the coverage of these measurements in L_s, latitude, longitude, and local time. The profiles shown in this paper are publicly available at https://atmos.nmsu.edu/data_and_services/atmospheres_data/MARS/tp.html.

2.2. MOC wide-angle images

MOC monitored the atmosphere from terminator to terminator on every orbit with its red (580–620 nm) and blue (400–450 nm) wide-angle (WA) cameras (Malin and Edgett, 2001; Cantor et al., 2002). Both cameras have a 2880-km-wide field of view in the cross-track direction. Images acquired in the daily global mapping mode have a resolution in most cases of 7.5 km/pixel, improving to 3.75 km/pixel during special campaigns. The results reported here are from the blue camera, which is more sensitive to clouds and less sensitive to dust than the red camera.

The annular cloud forms in early summer at a latitude where it is exposed to sunlight for most of the day; hence, it was visible to the WA cameras on most orbits. Our investigation benefits in two ways from the lighting conditions. First, it is possible to observe how the structure of the cloud varies with time of day. In addition, individual RO profiles can be interpreted in the context of nearly simultaneous WA images; the time delay between RO and MOC observations at the same location is only 6–8 min.

The WA images were projected onto a uniform 0.1° by 0.1° latitude-longitude grid and assembled into Mars Daily Global Maps (MDGMs) (Wang and Ingersoll, 2002). Each MDGM comprises a weighted average of WA images from

13 consecutive orbits. There is significant overlap among the images at high latitudes, where the Sun never sets. Within this region, the greatest weight is assigned to the image swath with the best lighting conditions (at a local time of 14 h). MDGMs are used here only for broad comparisons between the spatial distributions of polar clouds and NMLs. The MDGMs are publicly available (Wang, 2016).

3. Method of analysis

Fig. 1 illustrates the basic characteristics of the RO profiles used in this investigation. These are standard retrievals in which the atmosphere is assumed to be dry. One pair of profiles (blue) sounded the atmosphere at a location where a water-ice cloud appears in contemporaneous WA images (see Section 4.3). A temperature inversion forms in response to nighttime radiative cooling in the cloud layer (Fig. 1A), and the cooling is sufficient to trigger convective instability below the inversion, resulting in a mixed layer where θ is nearly constant (Fig. 1B) and its vertical derivative $d\theta/dz$ is close to zero (Fig. 1C). These features are absent from the other pair of profiles (orange), which sounded the atmosphere in cloud-free regions. The blue and orange profiles of θ differ by about 7 K at the base of the inversion (near 400 Pa), far larger than the measurement uncertainty of about 0.9 K. All four profiles have a temperature inversion and a high degree of static stability in the lowest kilometer above the surface, as expected at the local time of these measurements (4.8 h).

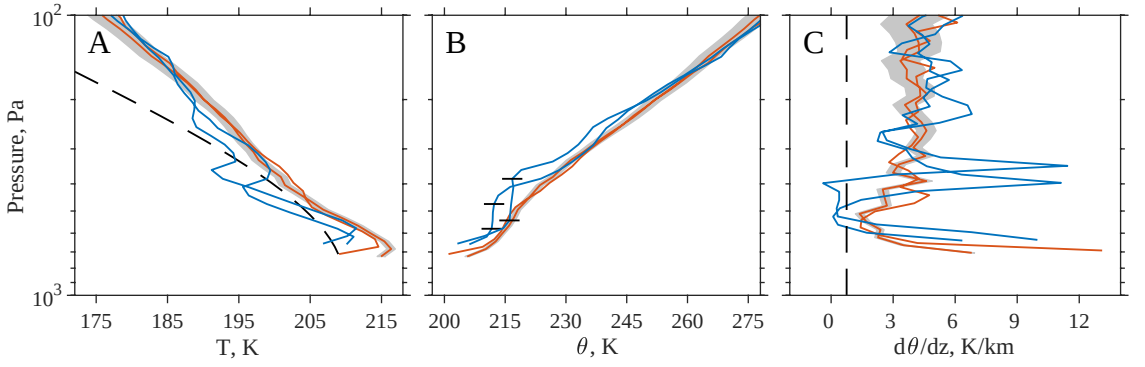

Figure 1: RO profiles of (A) T, (B) θ, and (C) $d\theta/dz$ from early summer (L_s = 123°) of MY27. The latitude (62°N) and local time (4.8 h) are the same in all profiles. The base of each profile is about 500 m above the surface. Profiles at longitudes of 220°E and 244°E (blue) contain an NML (where θ is nearly constant) with an overlying temperature inversion. These features are absent from profiles at 3°E and 89°E (orange). Gray shading shows the 1-σ uncertainty for the profile at 3°E; the accuracy of the other profiles is about the same. The dashed line in (A) is a model for the saturation temperature of water vapor. The black lines in (B) mark the upper and lower boundaries of the NMLs, which are 2.1 and 3.5 km deep. The dashed line in (C) at 0.75 K km^{-1} is used to identify the mixed layers.

The profiles in Fig. 1 do not account for the effects of water vapor. For this reason there is a small, positive bias in the profiles of $d\theta/dz$. (We focus on $d\theta/dz$ because of its importance in identifying NMLs, as discussed below.) This bias has two components. The first arises from the dependence of the RO profiles on the assumed composition of the atmosphere (see Section 2.1). Water is a highly refractive molecule at microwave frequencies (Thayer, 1974), so that it can have an appreciable effect on the retrieved profiles despite its relatively small mixing ratio. The magnitude of the bias depends on the vertical distribution of water vapor, which is not well known, so we use a simple model for illustration. The volume mixing ratio f is assumed to be a Gaussian function:

$$f(z) = f_o \exp\left(\frac{-z^2}{2\,h^2}\right) , \tag{1}$$

where z is the height above the surface, f_o is the mixing ratio at the surface, and h is the characteristic vertical scale. Fig. 1A shows the saturation temperature predicted by this model when f_o = 1000 ppmv and h = 5 km, which yields a column abundance (33 pr-μm) that matches TES measurements at this location and season (Smith, 2004). The model is consistent with the presence of a cloud layer at pressures of about 350–500 Pa in the profiles shown in blue and the absence of clouds (apart from ground fog) in the profiles shown in orange.

Independent measurements suggest that Eq. (1) is a plausible model. Pankine and Tamppari (2015) constrained the vertical distribution of water vapor at the Phoenix landing site (234°E, 68°N) through analysis of data from the MGS Thermal Emission Spectrometer. They found that water vapor is well mixed within 10 km of the surface and absent at higher altitudes in the early summer season (L_s = 110–140°). The model in Eq. (1) is generally consistent with this result; when h = 5 km, 70% of the water vapor is within 4 km of the surface and 99% is within 11 km.

We used the water-vapor model to retrieve a "wet" profile for each of the experiments shown in Fig. 1. The fundamental refractive index profile is now apportioned among CO_2, N_2, ^{40}Ar, and H_2O, resulting in slightly different profiles of T, p, and θ. The change in $d\theta/dz$ is largest near the top of the mixed layer, at a pressure of about 400 Pa, where its value is reduced by about 0.2 K km^{-1} relative to the dry profile. This affects all four profiles in the same way, regardless of whether a cloud is present.

The second component of the water-related bias arises from the release of latent heat, which was ignored in the calculation of θ. Its impact on static stability can be estimated by replacing θ with the equivalent potential temperature θ_e (Gill, 1982), as discussed in connection with a different set of RO profiles by Hinson et al. (2014, Section 4.1). For the observations in Fig. 1, $d\theta_e/dz$ is only slightly smaller than $d\theta/dz$. The magnitude of the change at pressures of 350–500 Pa (the cloud layer in the profiles shown in blue) is comparable to the change produced by the refractivity of water vapor. Profiles from cloud-free regions are unaffected by this type of bias.

The net effect of water vapor can be summarized as follows. Within an NML, the true value of $d\theta/dz$ is roughly 0.4 K km^{-1} smaller than the estimate derived from the dry profile. The bias is expected to be about half as large in cloud-free regions, where latent heating is absent. The corresponding bias to profiles of T and θ is of order 1 K, much smaller than the effect of cloud radiation, which is about 7 K at the top of the mixed layer (Fig. 1).

We identified NMLs through their effect on $d\theta/dz$, using a criterion based on a broad survey of RO profiles. For example, Fig. 2 shows histograms constructed from RO measurements within a 15° latitude band centered on 65°N. A different range of L_s was sampled in each year. One histogram (blue) displays the minimum value of $d\theta/dz$ from each profile. The median of this distribution decreases as L_s increases: 2.4 K km^{-1} at L_s = 70–100° (MY25), 2.1 K km^{-1} at L_s = 82–115° (MY26), and 1.5 K km^{-1} at L_s = 115–140° (MY27). This is a consequence of the seasonal evolution of the temperature structure within this latitude band. The second histogram (orange) is discussed below.

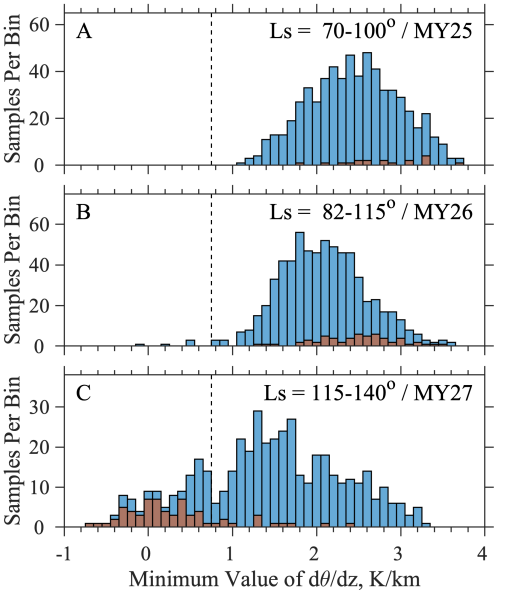

Figure 2: Histograms constructed from RO profiles acquired in (A) MY25, (B) MY26, and (C) MY27. All measurements are from a 15° latitude band centered on 65°N. The range of L_s varies from year to year. Each set of observations has complete coverage in longitude at a fixed local time of (A) 2.8 h, (B) 3.8 h, and (C) 5.1 h. The histograms show (blue) the minimum value of $d\theta/dz$ in each profile and (orange) the number of profiles in each bin with a temperature inversion that exceeds 0.5 K. The vertical dotted line at 0.75 K km^{-1} is used to identify NMLs.

The latitude band used in Fig. 2 is aligned with the center of the annular cloud, which forms each year at about $L_s = 120°$ and has a lifetime of 20–30 sols (10–15° of L_s) (Sánchez-Lavega et al., 2018). Hence, the cloud had not yet appeared at the time of the RO observations in MY25 and 26 (Fig. 2A and 2B), but it was present within the span of the observations in MY27 (Fig. 2C). (See Section 4.3 for contemporaneous MOC images of the cloud). The histogram in Fig. 2C is unique in that the minimum value of $d\theta/dz$ is less than 1 K km^{-1} in a significant number of profiles, 132 out of 461, as compared with only 11 out of 670 profiles in Fig. 2B and none in Fig. 2A. This low-stability tail in the distribution signals the presence of NMLs; as we show in Section 4.3, most of the profiles with NMLs are from within the annular cloud. Moreover, there is a local minimum in the bin centered at 0.8 K km^{-1} in Fig. 2C, and we adopt the lower boundary of this bin (0.75 K km^{-1}) as the threshold that separates ordinary profiles and those with NMLs. By this definition, a profile in which all samples of $d\theta/dz$ exceed 0.75 K km^{-1} does not contain an NML (e.g., the orange profiles in Fig. 1C). In all other profiles, the NML comprises the layer where $d\theta/dz$ is less than 0.75 K km^{-1} (e.g., the blue profiles in Fig. 1C). As explained above, the true value of $d\theta/dz$ in the mixed layer may be smaller by as much as 0.4 K km^{-1} than the estimate derived from the dry profile, owing to the effects of water vapor, so that the threshold is closer to neutral stability than it first appears.

We also searched for temperature inversions that might indicate the presence of a water ice cloud. The search was limited to altitudes below 15 km AGL and above the shallow layer adjacent to the surface, where an inversion appears in all early morning RO profiles. We refer to inversions by their magnitude, defined as the change in temperature across the layer where $dT/dz > 0$. Inversions that exceed 0.5 K are relatively rare, as shown by the second histogram in Fig. 2 (orange bars). Nonetheless, there is a significant correlation between NMLs and temperature inversions for the measurements in Fig. 2C—inversions that exceed 0.5 K are present in 51% of the profiles that contain an NML but only 4% of the other profiles. In the discussion that follows, the evidence for cloud-induced convection is considered to be strongest when an NML is accompanied by an inversion that exceeds 0.5 K.

However, not all inversions are associated with NMLs. For example, only 1% of the profiles in Fig. 2B contain an NML, whereas 10% have an inversion that exceeds 0.5 K. Most of these inversions appear in profiles where the minimum value of $d\theta/dz$ exceeds 2 K km^{-1} and an NML is definitely not present. Within this set of observations, the inversions are centered at 4.1 $\pm$ 1.2 km AGL, near the top of the daytime convective boundary layer at the Phoenix landing site (Whiteway et al., 2009), which suggests a possible explanation. The daytime mixed layer is sometimes capped by a subsidence inversion (Hinson et al., 2019), and remnants of this structure could persist into the night even after the lower atmosphere has returned to stable stratification.

4. Results

Section 4.1 surveys the RO profiles used in this investigation and summarizes the distribution of NMLs in season, latitude, and longitude. Three time periods are selected for more detailed analysis, with boundaries that reflect the seasonal evolution of the polar clouds. Section 4.2 briefly discusses results from the season in which NMLs first appear in significant numbers. Section 4.3 closely examines the annular cloud and the dense cluster of NMLs that form in response to its radiative effects. Section 4.4 focuses on subsequent observations of NMLs that appear in connection with an eastward-moving frontal cloud.

4.1. General distribution of NMLs

The annular cloud forms each year in early summer directly north of Alba Mons in Vastitas Borealis. RO measurements at this location and season are available from three successive years (MY25–27), as shown in Fig. 3A. These occultations sounded the atmosphere at latitudes of 48–85°N and local times of 3–9 h. In all 3 years the observations begin at lower latitudes in late spring, well before the annular cloud appears, and end at higher latitudes in late summer, well after the cloud is gone. The local time advances steadily as L_s increases, starting at about 3 h and ending at about 9 h in each year. The observations are widely distributed in longitude, as shown in subsequent figures.

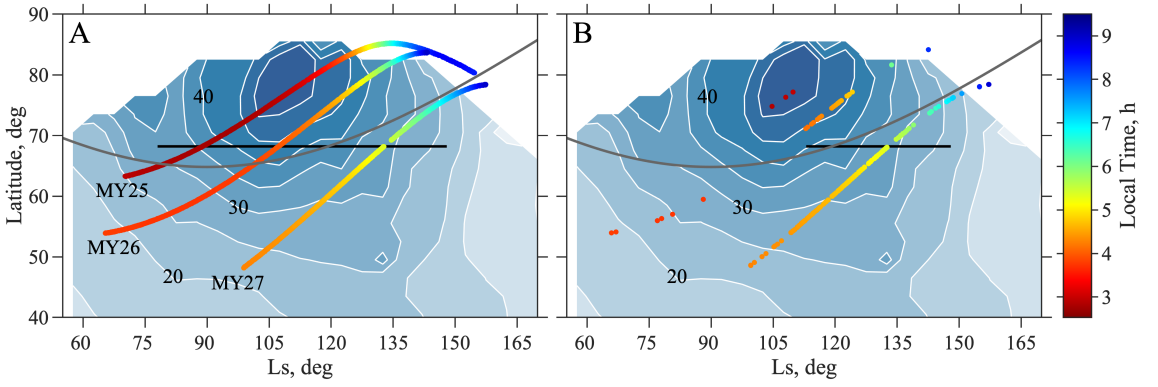

Figure 3: (A) The distribution in L_s, latitude, and local time (color shading) of RO profiles from MY25, 26, and 27. The contour plot shows the zonal-mean water-vapor column abundance observed by TES in MY26. Contours are shown at intervals of 5 pr-μm, with labels at 20, 30, and 40 pr-μm. The curving gray line is the southern boundary of the region that experiences polar day. The horizontal black line marks the latitude and duration of the Phoenix mission in MY29. (B) Distribution of RO profiles that contain an NML. The horizontal black line now shows the time span when a detached, nighttime cloud layer was observed by the Phoenix LIDAR.

Many aspects of Martian weather are highly repeatable at the location and season considered here (Cantor et al., 2002; Liu et al., 2003; Smith, 2004; Wang and Fisher, 2009; Wilson and Guzewich, 2014). In the context of this investigation, the most important example is the annular cloud. It appears every year at essentially the same season and location (Malin et al., 2010; Sánchez-Lavega et al., 2018), implying a high degree of repeatability in both the basic state of the atmosphere (temperature and water vapor abundance) and the dynamics (a low pressure system). In analyzing the RO observations, we therefore assume that interannual variations can be ignored. This makes it possible to examine the spatial distribution and seasonal evolution of the NMLs by combining RO results from different years, which sampled the same latitude at different seasons (as in Fig. 2) and the same season at different latitudes.

Fig. 3B shows the meridional and seasonal distribution of RO profiles that contain an NML and compares it with results from the Phoenix LIDAR. During the second half of the Phoenix Mission, the LIDAR detected a 500-m layer of ground fog as well as a detached cloud layer positioned about 4 km AGL (Whiteway et al., 2009; Dickinson et al., 2010). Both appeared only at night. The cloud layer followed a regular diurnal cycle, forming at a local time of about 1 h and largely dissipating by about 9 h. It was first observed at $L_s = 113°$, and it was present in all subsequent observations, which continued until about $L_s = 147°$. (As discussed by Dickinson et al. (2010, Fig. 3), relatively few nighttime observations are available after $L_s = 133°$.) All RO observations considered here fall within the range of local time when the cloud layer was present above the Phoenix landing site. Most of the NMLs appear in the same seasonal window as the Phoenix cloud—in the combined measurements from MY25–27, 84% of the NMLs were observed between $L_s = 108°$ and $L_s = 140°$.

NMLs are most common in measurements from MY27, appearing in 15% of 1084 profiles, and far less common in those from MY26 (1.7% of 1555 profiles) and MY25 (0.3% of 1518 profiles), as shown in Fig. 3B. Taken together, the RO observations from the three years imply that NMLs are restricted to lower latitudes, well away from the peak in the water-vapor column abundance. This point is illustrated by measurements at $L_s = 108$–$118°$, when there is a strong meridional gradient in the abundance of water vapor. At this season, NMLs are most common in the measurements at lower latitudes in MY27 (20% of 199 profiles), where the zonal-mean column abundance of water vapor is relatively small (less than 30 pr-μm). Conversely, few NMLs were detected at higher latitudes in MY26 (3.9% of 181 profiles) or MY25 (1.2% of 172 profiles), where the zonal-mean column abundance of water vapor is much larger (more than

45 pr-μm).

The NMLs are not distributed uniformly in longitude, and their zonal distribution evolves with time; Fig. 4 shows results from MY27. NMLs first appear in significant numbers at L_s = 108–118°, when they are spread across the western hemisphere (180–360°E). In subsequent observations at L_s = 118–133°, the NMLs are concentrated in a narrower range of longitude (220–320°E), where overlying inversions of at least 0.5 K are common. The distribution then shifts eastward at L_s = 133–140° (300–120°E). As we show in Sections 4.3 and 4.4, the zonal distribution of NMLs is correlated with specific clouds observed by MOC, which are also confined in longitude. These three spans of L_s are bounded by gray lines in Fig. 4; they contain 86% of the NMLs observed in MY27 as well as most of the NMLs observed in MY25 and 26. The observing conditions are summarized in Table 1.

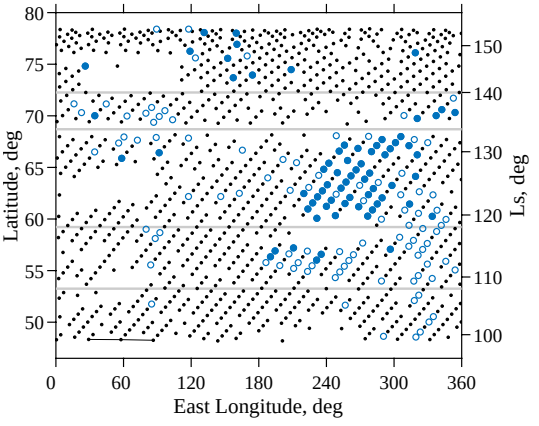

Figure 4: The distribution of NMLs in longitude, latitude (left ordinate), and L_s (right ordinate) in MY27. A black dot marks the location of each RO profile, a blue open circle denotes the presence of an NML, and a blue filled circle denotes the presence of an NML with an overlying temperature inversion that exceeds 0.5 K. The black line at the lower left connects observations from three successive orbits. Larger gaps in longitude occur when DSN tracking was not available. Gray lines mark boundaries between subsets of data discussed in Sections 4.2–4.4. The axis labels on the right ordinate are not uniformly spaced because the dependence of latitude on L_s is not linear (see Fig. 3A).

Table 1
Summary of RO observations in the seasonal windows discussed in Sections 4.2–4.4.

MY	L_s	Latitude	Local Time	Solar Elevation	Number of Profiles	Number of NMLs
25	108–118°	76–81°N	2.9–3.4 h	14–16°	172	2
26	108–118°	69–74°N	4.0–4.4 h	12–15°	181	7
27	108–118°	53–59°N	4.4–4.6 h	6–9°	199	40
25	118–133°	81–85°N	3.4–6.1 h	16–18°	245	0
26	118–133°	74–81°N	4.4–6.0 h	15–18°	268	13
27	118–133°	59–68°N	4.6–5.4 h	9–13°	295	83
25	133–140°	85°N	6.2–7.9 h	18°	112	0
26	133–140°	81–83°N	6.0–7.8 h	18–19°	126	1
27	133–140°	69–72°N	5.5–6.0 h	14–15°	107	17

4.2. Early summer NMLs (L_s = 108–118°)

Wang and Fisher (2009) examined north-polar MDGMs from the spring and summer seasons of MY24–28 and assembled a catalog of clouds and dust storms with a front-like morphology. This type of activity occurs in spring and mid-to-late summer with an intervening gap in early summer whose exact timing varies from year to year. The hiatus ended at L_s = 123°, 115°, 111°, and 113° in MY25–28, respectively. The end of the hiatus coincides with the arrival

of a nighttime cloud layer above the Phoenix landing site at L_s = 113° of MY29 (Whiteway et al., 2009; Dickinson et al., 2010).

This subset of RO observations is from a transitional season (L_s = 108–118°) between the hiatus in frontal activity and the appearance of the annular cloud. NMLs were detected in significant numbers (Fig. 3B), primarily in observations at lower latitudes from MY 27 (53–59°N), as summarized in Table 1. Among the 40 NMLs identified in MY27, 90% are at longitudes of 180–360°E (Fig. 4). Their average depth is 1.1 km and their altitude is typically 5–6 km AGL, corresponding to a pressure of about 450 Pa. A few outliers at longitudes of 248–264°E appear at higher altitudes, about 11 km AGL. Only 9 NMLs were found in the high-latitude observations from MY26 (69–74°N) and MY25 (76–81°N); they appear at longitudes of 268–324°E, more than 30° east of the Phoenix landing site.

Wang and Fisher (2009) reported the presence of arc-shaped water-ice clouds during this seasonal window at latitudes of 55–75°N and longitudes of 225–315°E, within the longitude band where NMLs were detected. This suggests that frontal clouds are the source of the NMLs. However, the lighting conditions were unfavorable in this subset of RO observations, particularly in MY27 when the Sun was only 6–9° above the horizon. For this reason we did not attempt to correlate individual NMLs with clouds appearing in WA image swaths from the same orbit.

4.3. The annular cloud (L_s = 118–133°)

This season is particularly interesting because of the presence of the annular cloud. NMLs were observed frequently at locations within the cloud, and the cloud was visible to MOC at a wide range of local times.

During this time period, NMLs are most common in measurements at lower latitudes and entirely absent at the highest latitudes, as shown in Fig. 5A. They are present in 28% of the profiles at 59–68°N (MY27), 5% of the profiles at 74–81°N (MY26), and none of the profiles at 81–85°N (MY25). Moreover, the NMLs appear routinely in a 120° longitude band centered at about 270°E but only rarely at other longitudes. The local time was about 5 h in all three years (Table 1).

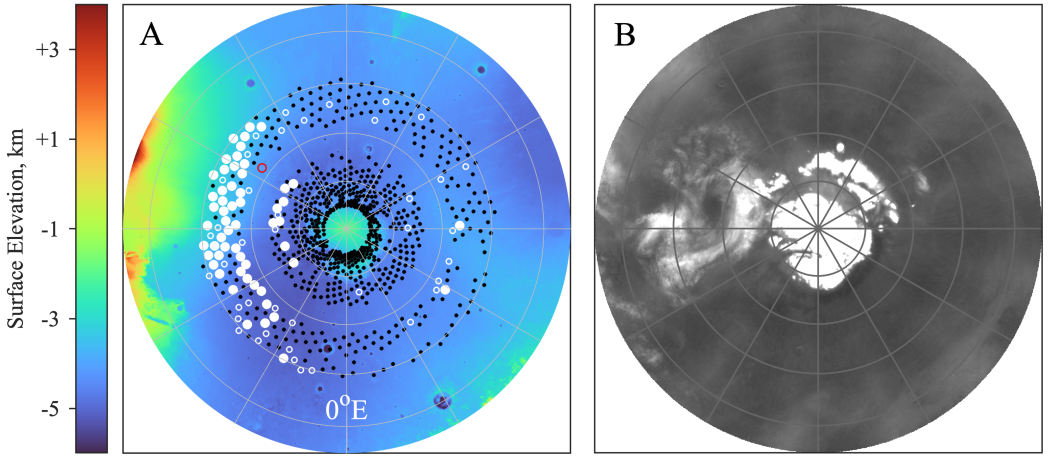

Figure 5: (A) The spatial distribution of NMLs at L_s = 118–133° superimposed on a map of surface elevation. This is a composite of RO measurements from three years: 59–68°N in MY27, 74–81°N in MY26, and 81–85°N in MY25. A black dot marks the location of an ordinary RO profile, a white open circle denotes the presence of an NML, and a white filled circle signifies an NML with an overlying temperature inversion that exceeds 0.5 K. Parallels are shown at 10° intervals from 50°N to 80°N. A red circle marks the Phoenix landing site. (B) MOC MDGM (blue camera) from L_s = 119.8° of MY27. The annular cloud is to the left of the residual water-ice cap.

The spatial distribution of the NMLs is correlated with the location of the annular cloud, as shown in Fig. 5. The MDGM in Fig. 5B is from L_s = 119.8° of MY27, contemporaneous with the RO measurements at 59–68°N. But the cloud structure observed in MY27 is also well aligned with the NMLs observed at 74–81°N in MY26, owing to the close resemblance between the annular clouds observed in the two years (Malin et al., 2010, Fig. 35). As discussed in Section 2.2, the information in the MDGM comes primarily from the dayside segment of the WA image from each orbit, where the local time is about 14 h. Later in this section we examine single-orbit image swaths to characterize the diurnal cycle and day-to-day variability of the cloud as well as its appearance at the local time of these RO measurements (about 5 h).

A closer look at the zonal distribution of the NMLs confirms their association with the annular cloud. We sorted the data from L_s = 118–133° of MY27 into 15° longitude bins and compared the number of NMLs with the total number of profiles. Fig. 6A shows the results. NMLs are most common at 240–285°E, where they appear in more than 75% of the profiles. This is well aligned with the longitude range of the annular cloud (Fig. 5B). The zonal distribution of NMLs is somewhat broader than the daytime extent of the cloud, possibly because of the evolution of the cloud during the 30-sol span of these RO observations.

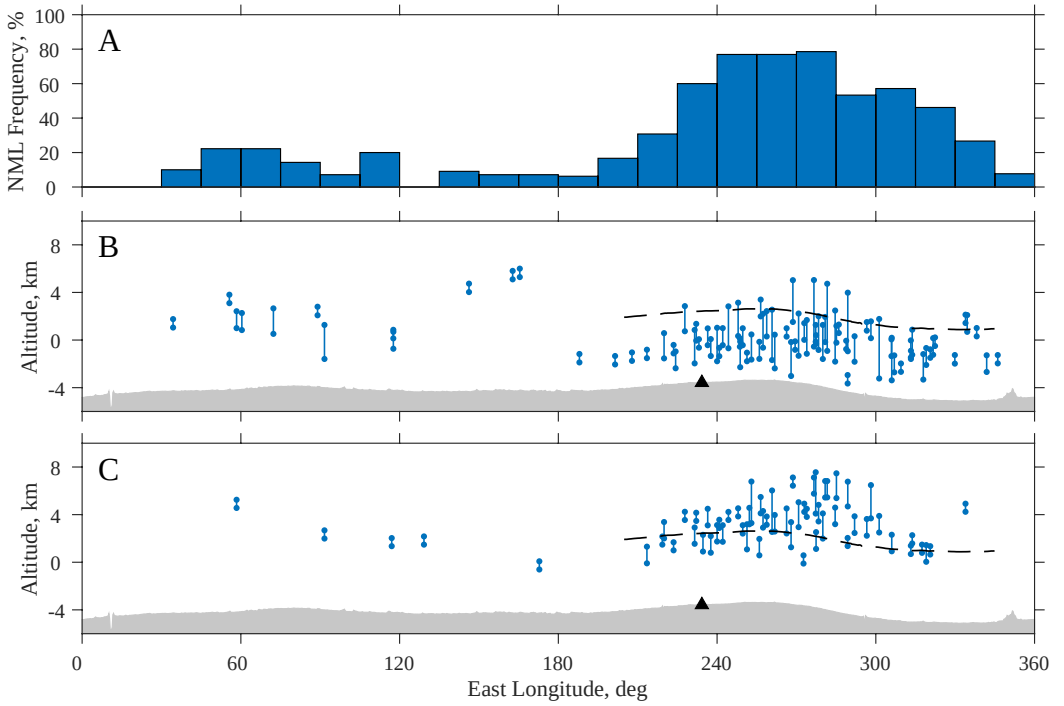

Figure 6: Results derived from RO observations at 59–68°N during L_s = 118–133° of MY27. The bar chart in (A) shows the percentage of profiles with NMLs in each of 24 equally spaced longitude bins. The other panels show the distribution in longitude and altitude of (B) NMLs and (C) temperature inversions that exceed 0.5 K; altitude is measured from the areoid. Each feature is indicated by a line connecting its lower and upper boundaries. In both (B) and (C), a black triangle marks the longitude of the Phoenix landing site, gray shading shows the surface elevation at 64°N, and the dashed line is 6 km AGL.

Within the observations at L_s = 118–133° of MY27, there are 71 NMLs at longitudes of 180–360°E, in the vicinity of the annular cloud. Some are as shallow as 0.7 km while others are as deep as 5.6 km, as shown in Fig. 6B. On average, the top of the NML is 4.9 km AGL, at the 470-Pa pressure level; the corresponding numbers at the base of the NML are 3.0 km and 560 Pa. Hence, most NMLs form within the same altitude range as the water-ice cloud layer detected by the Phoenix LIDAR, which appeared at a height of about 2–5 km AGL in observations at the same local time and season of MY29 (Dickinson et al., 2010, Fig. 4). However, 16 of the NMLs at 180–360°E extend to a height of more than 6 km AGL. The most conspicuous cases are at longitudes of 268–290°E, where four NMLs reach heights of 8.2–8.7 km AGL. This is comparable to the cloud-top height of 10 ± 3 km derived from spacecraft images of the annular cloud (Sánchez-Lavega et al., 2018).

Like the NMLs in Fig. 6B, temperature inversions that exceed 0.5 K form primarily in the annular cloud. Inversions of this magnitude appear directly above 49 of the 71 NMLs at 180–360°E, as shown in Fig. 6C. On average, the top of the inversion is 8.1 km AGL (340 Pa), the base of the inversion is 6.6 km AGL (390 Pa), and the magnitude of the inversion is 2.6 K. The top of the NML and the base of the inversion are expected to be roughly aligned with the level of maximum radiative cooling by the cloud.

The spatial and temporal variability in the structure of the NMLs is illustrated in Fig. 7. It shows two, 1-sol sequences of RO profiles from MY27, one centered at $L_s = 119.8°$ and the other at $L_s = 128.2°$. There are three NMLs in each group of profiles; their depth and vertical extent vary widely with longitude on each sol and the structure of the NMLs also changes significantly in the 16-sol interval between the two sets of profiles. A few of the orange profiles appear to be perturbed by cloud-induced radiative cooling, most notably the one at 219°E in Fig. 7A; it contains a 1.4-K temperature inversion centered at the 420-Pa pressure level but the minimum value of $d\theta/dz$ slightly exceeds the threshold used to identify the NMLs.

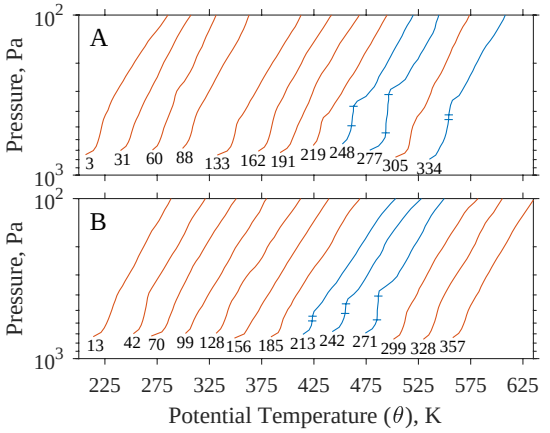

Figure 7: Two sets of RO profiles, each from a 1-sol sequence of observations. (A) Twelve profiles from $L_s = 119.6$–$120.0°$ (MY27) at 60.3°N; the local time is 4.7 h. (B) Thirteen profiles from $L_s = 128.0$–$128.4°$ (MY27) at 65.5°N; the local time is 5.1 h. The number at the base of each profile is the east longitude of the measurement, which moves westward by 28.6° per spacecraft orbit. For clarity, an offset equal to the measurement longitude has been added to each profile of θ. Color indicates the presence (blue) or absence (orange) of an NML. The upper and lower boundaries of each NML are marked by horizontal lines. These six NMLs are part of the distribution shown in Fig. 6B.

The variability in the properties of the NMLs may be a consequence of the complex morphology of the annular cloud. Sánchez-Lavega et al. (2018) report that the character of the cloud sometimes varies widely across a single image, with arc-spiral bands accompanied by what appear to be thin cirrus, thick stratus, and altocumulus clouds. The infrared emissivity of the cloud will vary accordingly, with a direct impact on the properties of the NMLs. A deep NML is expected to form where the emissivity is large, owing to the the resulting increase in the radiative cooling rate. Conversely, the NML will be shallow where the emissivity is small.

The appearance of the annular cloud varies dramatically with local time, as illustrated in Fig. 8. When viewed at a local time of about 5 h (Fig. 8H), the portion of the cloud within the image has a well defined circular boundary, a diameter of about 1300 km, and a compact clear center at 258°E, 68°N. The cloud subsequently dissipates (Fig. 8I–8L), and by late afternoon it has lost its symmetry, the clear center has greatly expanded, and the overall structure resembles a crescent (Fig. 8A and 8B). See Cantor et al. (2002) for MOC images showing the daytime evolution of the annular cloud in MY24.

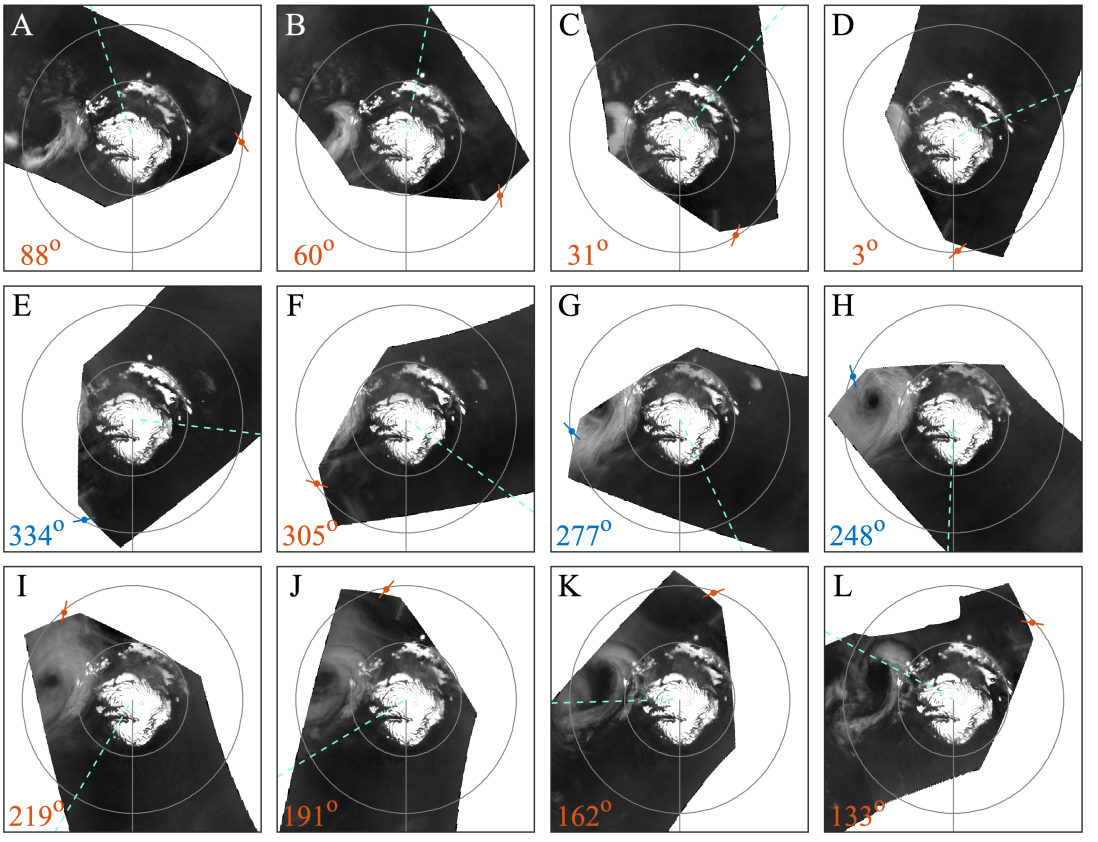

Figure 8: MOC WA images (blue camera) from 12 consecutive orbits centered on L_s = 119.8° of MY27. The annular cloud appears to the left of the residual water-ice cap in each panel. An RO experiment was performed less than 8 min after completion of each image swath; the location is marked by a dot in each panel, with a line to indicate the horizontal resolution along the direction from spacecraft to Earth. Color coding indicates the presence (blue) or absence (orange) of an NML. The corresponding RO profiles appear in Fig. 7A. The latitude (60.3°N) and local time (4.7 h) are the same for all RO measurements; the east longitude is specified at the lower left in each panel. The dashed line is the subsolar longitude at the time of the RO observation. The prime meridian is shown in gray, along with parallels at 60°N and 75°N.

Fig. 8 places the RO profiles into context with nearly simultaneous observations of cloud structure. An RO experiment sounded the atmosphere near the terminator on all 12 orbits; the location is indicated in each panel of Fig. 8. The time delay between MOC and RO observations on the same orbit is negligible, less than 8 min. Successive RO measurements moved westward by 28.6° but the latitude (60.3°N) and local time (4.7 h) remained constant. The RO profiles from these 12 orbits are shown in Fig. 7A. Relatively deep NMLs are present when the RO experiment sounded the atmosphere within the annular cloud (Fig. 8G and 8H), and a shallow NML appears at 334°E, adjacent the cloud (Fig. 8E). Conversely, NMLs are absent at longitudes far away from the cloud. As noted previously, the RO profile at 219°E appears to be perturbed by cloud-induced radiative cooling (Fig. 7A). The location of the measurement near the western edge of the annular cloud (Fig. 8I) is consistent with this conclusion.

We examined additional MOC images like the ones in Fig. 8 and found that the diurnal cycle of the annular cloud persists for several sols. A 5-sol animation centered on L_s = 120° is included as supplementary material in Appendix A. The results are summarized in Fig. 9. The magnitude of the diurnal cycle is reflected in the large difference between

the two images in each row, which show the cloud structure (left) in the afternoon and (right) in the early morning of the following sol. But the diurnal cycle is largely the same on all 4 sols, as evidenced by the similarities among the images in each column, which show the cloud structure at about the same local time on successive sols. The cloud is more extensive and closer to circular symmetry in the early morning (right column) but dissipates during the day (left column), especially at lower latitudes, where the diurnal variations are more pronounced. The images in Fig. 9B, 9D, 9F, and 9H show the appearance of the annular cloud at the local time of the RO measurements in Fig. 5.

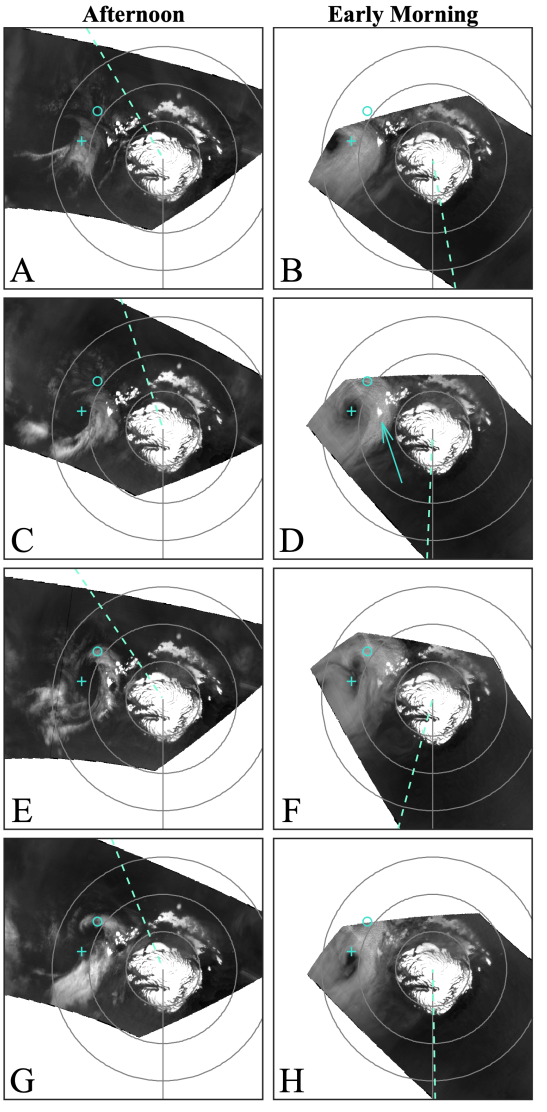

Figure 9: MOC WA images from L_s = 119–121° of MY27. The interval between successive frames is about half a sol. The subsolar longitude is indicated by a dashed line. The prime meridian is shown in gray, along with parallels at 60°N, 70°N, and 80°N. The north pole is offset from the center of the image to show the daytime structure of the annular cloud at lower latitudes. The open circle is the Phoenix landing site. The cloud is centered at 258°E, 68°N in (D); this location is marked by a plus symbol in each panel for reference. A bright surface feature, identified by an arrow in (D), is visible through the cloud. The approximate local time at the center of the annular cloud is (left) 15.5 h and (right) 5.5 h.

The center of the annular cloud shifted northward by about 270 km in the 1-sol interval between Fig. 9B and 9D, and it remained at about the same latitude on the next two sols. Its movement in longitude is difficult to track precisely, owing to asymmetry near the center of the cloud in Fig. 9F and 9H, but its average speed in the zonal direction was smaller than 1 m s^{-1} during this 4-sol span. This behavior can be compared with results reported by Sánchez-Lavega

et al. (2018, Table 1 and Fig. 3), who analyzed a 9-sol sequence of observations at L_s = 125–129° of MY31, when a double cyclone was present. Both vortices exhibited oscillatory motion in latitude while generally traveling eastward at a typical speed of 3–5 m s^{-1}. Interestingly, the trailing cyclone was initially centered at about 260°E, and it moved northward with relatively little change in longitude on the first few sols of this sequence, much like the single cyclone observed at L_s = 119–121° of MY27 (Fig. 9).

The nighttime cloud layer observed by the Phoenix LIDAR had an (extinction) opacity of about 0.1 at 532 nm Dickinson et al. (2010). This is qualitatively consistent with the cloud shown in Fig. 9, as implied by the presence of a bright surface feature, identified by an arrow in Fig. 9D, that remains visible throughout the diurnal cycle of the cloud.

Additional information is available from MCS, the nine-channel, infrared, filter radiometer onboard Mars Reconnaissance Orbiter. MCS has been monitoring the Martian atmosphere since MY28, yielding profiles of temperature, dust opacity, and water-ice opacity with daily global coverage at local times of 3 and 15 h (McCleese et al., 2007, 2010; Kleinböhl et al., 2009, 2011). The 5-km vertical resolution of the MCS profiles is not sufficient for direct observations of the thin cloud layers, NMLs, and temperature inversions considered here. Nonetheless, MCS measurements provide valuable context for interpreting the results in Figs. 8 and 9.

We analyzed MCS profiles from early summer of several years and characterized the variations in air and surface temperature that control the diurnal cycle of the annular cloud. This discussion is limited to results from L_s = 120–130° of MY29, which are sufficient to illustrate the main points. At latitudes of 65–70°N, near the center of the cloud, the zonal-mean temperature at 419 Pa (about 6 km AGL) increases from 204 K at 3 h to 212 K at 15 h. The zonal-mean surface temperature in the same latitude band increases from 193 K at 3 h to 249 K at 15 h; hence, the intensity of infrared radiation emitted by the surface changes by nearly a factor of three from night to day. The cloud will dissipate during the day, when the boundary layer is relatively warm and the cloud is heated by long-wave radiation from the surface. At night, the boundary-layer temperature is closer to saturation, and with the large decrease in surface temperature, the cloud emits more infrared radiation than it absorbs, reducing the local air temperature and promoting cloud formation.

4.4. Eastward-traveling frontal clouds (L_s = 133–140°)

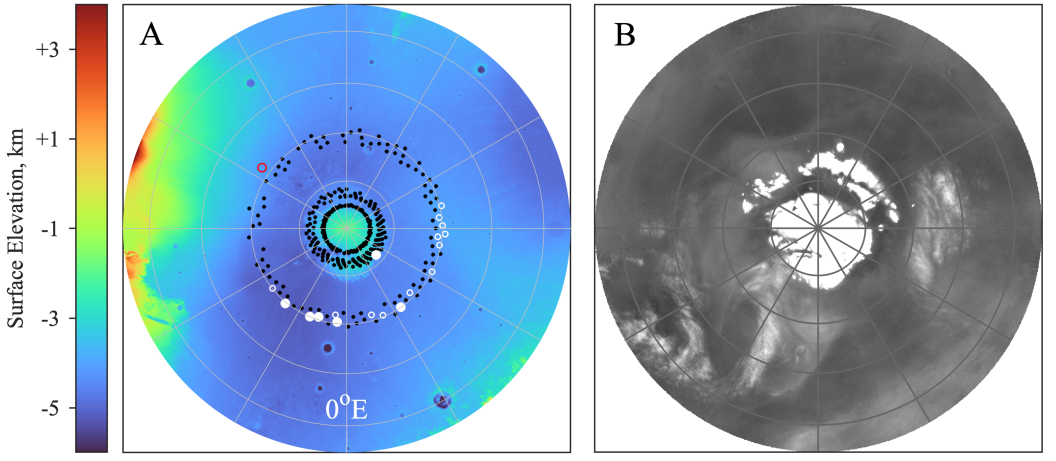

Figure 10: (A) The spatial distribution of NMLs at L_s = 133–140° superimposed on a map of surface elevation. The RO measurements sampled a different range of latitude in each year: 69–72°N in MY27, 81–83°N in MY26, and 85°N in MY25. The symbols are the same as in Fig. 5. (B) MOC MDGM from L_s = 135.7° of MY27. The annular cloud is no longer present; a frontal cloud appears at 330–340°E.

As in the preceding time period, NMLs form at locations where water-ice clouds are present. However, the nature of the clouds and the spatial distribution of the NMLs have changed in response to the seasonal evolution of atmospheric dynamics, as shown in Fig. 10. NMLs are again most common at lower latitudes (Table 1); they appear in 16% of the profiles at 69–72°N (MY27), 1% of the profiles at 81–83°N (MY26), and none of the profiles at 85°N (MY25). But their zonal distribution has shifted eastward relative to those in Fig. 5; NMLs are now confined to a 180° longitude band centered at about 30°E (cf. Fig. 4). Their distribution in longitude is not uniform—there is a noticeable cluster of

NMLs near 90°E, whereas NMLs with inversions that exceed 0.5 K are most common at 320–360°E. The observing conditions were slightly different than in the preceding time period; the Sun was higher above the horizon (14–19°) and the local time was later (5.5–7.9 h).

The MDGM in Fig. 10B was acquired at L_s = 135.7° of MY27, contemporaneous with the RO measurements at 69–72°N. Two types of clouds are present at the latitudes sampled by those RO profiles. One is centered at about 90°E, north of Utopia Planitia; it appears each year at about the same location and season (Wang and Fisher, 2009) though it is not clear what causes it to form. The second is an eastward-moving frontal cloud at about 335°E. NMLs appear in the vicinity of both clouds. In this section we focus on the frontal cloud and its effect on the RO profiles.

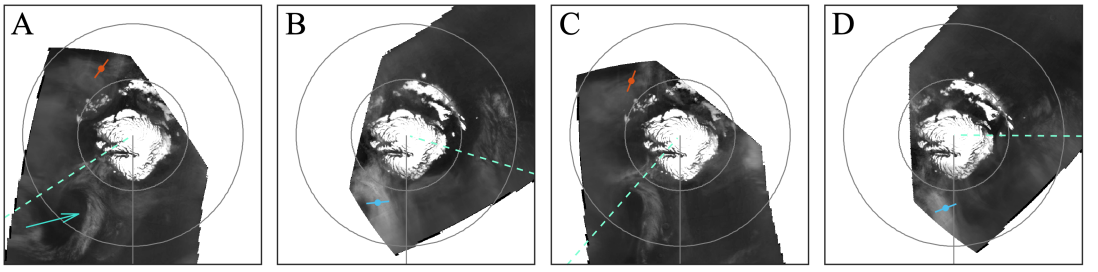

Figure 11: A 2-sol sequence of MOC WA images centered on L_s = 136° of MY27. A frontal cloud appears in each frame; its location is shown by an arrow in (A). The interval between alternate frames, (A)-(C) and (B)-(D), is about 1 sol. An RO experiment sounded the atmosphere within each image; its location is marked by a dot with a line that shows the horizontal resolution along the direction from spacecraft to Earth. Color denotes the presence (blue) or absence (orange) of an NML. The RO profiles appear in Fig. 12. The latitude (70.0°N) and local time (5.6 h) are the same in all four cases; the longitudes are (A) 206°E, (B) 337°E, (C) 223°E, and (D) 354°E. The subsolar longitude at the time of the RO observation is indicated by a dashed line. The prime meridian is shown in gray, along with parallels at 60°N and 75°N.

The frontal cloud travels slowly eastward, as shown in Fig. 11. The leading edge of the cloud shifts by roughly 10° in longitude during the 1-sol interval between Fig. 11A and 11C. Apart from this eastward motion, there is little change in the appearance of the cloud on successive sols at the same local time. As with the annular cloud, the frontal cloud is more substantial on the nightside (Fig. 11B and 11D) than on the dayside (Fig. 11A and 11C).

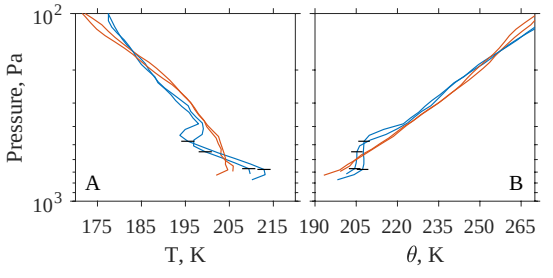

Figure 12: RO profiles of (A) T and (B) θ from a 2-sol span centered at L_s = 136° of MY27. An NML is present in the pair of profiles (blue) that sounded the atmosphere within the frontal cloud at the locations indicated in Fig. 11B and 11D (337°E and 354°E). The boundaries of the NMLs are marked by horizontal black lines. The other two profiles (orange) are from the locations indicated in Fig. 11A and 11C (206°E and 223°E).

Coordinated analysis of the MOC and RO data again provides compelling evidence that NMLs originate from water-ice clouds. Each MOC observation in Fig. 11 was accompanied by an RO experiment, which sounded the atmosphere at a location within the image. The time delay between the pair of observations on each orbit was only 6 min. Fig. 12 shows the four RO profiles of T and θ. The radiative effect of the frontal cloud is apparent in the profiles at 337°E and 354°E (Fig. 11B and 11D), which contain an NML and an overlying temperature inversion. The base of both NMLs is 1.7 km AGL, their depths are 2.2 and 3.6 km, and the inversions have magnitudes of 2.2 and 4.3 K. These features are absent from the other two RO profiles, which sampled the atmospheric structure at 206°E and 223°E, far away from the front (Fig. 11A and 11C). There is little difference between the temperature structure observed at nearly the same longitude on successive sols.

There are substantial differences in the temperature of the blue and orange profiles in Fig. 12. At the 450-Pa pressure level, the blue profiles are about 6 K colder than the orange profiles, owing to radiative cooling in the frontal cloud. Conversely, the blue profiles are about 6 K warmer than the orange profiles at the 700-Pa pressure level (near the base of the NMLs); this is probably a consequence of near-surface advection of warm air from lower latitudes. By reducing the static stability of the lower atmosphere, the increase in temperature near the surface is conducive to the formation of an NML. This contrasts with the temperature structure in the annular cloud, where profiles with NMLs are colder than those without NMLs at pressures of 600–700 Pa (e.g., Fig. 1).

5. Summary and discussion

We have identified NMLs at high northern latitudes through analysis of RO profiles acquired in spring and summer of three successive years (MY25–27). Until now this type of mixed layer had been observed only in the tropics. Results include basic properties of the NMLs, such as the pressure, temperature, and altitude at their upper and lower boundaries, as well as constraints on their horizontal distribution and seasonal evolution. The polar NMLs are most common at latitudes of 53–72°N and longitudes of 210–330°E (Section 4.1). This reflects the spatial distribution of the water-ice clouds in which they form. The close connection between NMLs and polar clouds is demonstrated most clearly through orbit-by-orbit comparisons between RO profiles and MOC images (Figs. 8 and 11). Most of the NMLs considered here are associated with the annular cloud (Section 4.3); others appear within eastward-traveling frontal clouds (Section 4.4). Models suggest that both types of clouds arise from large-scale weather systems in Vastitas Borealis (Tyler and Barnes, 2014).

The NMLs associated with the annular cloud typically form at a height of 3–5 km AGL; the corresponding pressure range is 560–470 Pa. Most of these NMLs are capped by a temperature inversion that exceeds 0.5 K. On average, the inversion extends from 390 Pa (6.6 km AGL) to 340 Pa (8.1 km AGL), with an average magnitude of 2.6 K. However, the properties of both the NMLs and the overlying inversions vary widely with longitude and from sol-to-sol (Figs. 6B, 6C, and 7), possibly in connection with the complex internal structure and evolution of the cloud system. For example, the depth of the NMLs ranges from less than 1 km to more than 5 km, and the upper boundary of some NMLs extends to nearly 9 km AGL. The NMLs nearest the Phoenix landing site are centered about 4 km AGL, consistent with the cloud layer observed under similar conditions by the LIDAR (Whiteway et al., 2009; Dickinson et al., 2010). A table that summarizes the results from MY27 is available as supplementary data in Appendix A.

Spiga et al. (2017) used an LES to investigate the radiative and dynamical effects of the cloud layer above the Phoenix landing site. They found that a 2.5-km-deep mixed layer will form in response to nighttime radiative cooling by the water-ice clouds. The results reported here strongly support this conclusion by revealing that NMLs appear routinely within the annular cloud, including near its western boundary above the landing site (Fig. 5); their vertical structure (Fig. 6B) is similar to the mixed layer in the LES.

The LES provides unique insight into aspects of the cloud-induced dynamics, such as the vertical transport of water vapor and ice, that cannot be measured directly. Adiabatic cooling in the vapor-rich updrafts leads to condensation, which increases the emissivity of the cloud and the amount of infrared radiation it emits. The resulting decrease in air temperature generates negative buoyancy, which sustains the eddy mixing in a self-reinforcing cycle. Interestingly, the ice-rich downdrafts reach speeds of 2 m s^{-1}, sufficient to generate localized "snow storms" that extend below the base of the cloud. The virga-like structures observed by the LIDAR (Whiteway et al., 2009) could arise from these microbursts.

The appearance of the annular cloud depends strongly on time of day, as shown in Figs. 8 and 9. The area covered by the cloud is largest at the local time of the RO measurements in Figs. 5–7 (about 5 h) and smallest in the afternoon. We used MCS measurements to place the evolution of the cloud into context with the diurnal cycles of air and surface temperature. The dissipation of the cloud in late morning and early afternoon is probably a consequence of enhanced emission of infrared radiation by the surface and the daytime increase in boundary-layer temperature.

There may also be a diurnal cycle to the dynamics of the low-pressure system that gives rise to the annular cloud. The wind field is well organized at night, as implied by the circular symmetry of the cloud and its compact, clear center (Fig. 8H). Conversely, the cloud structure, and presumably the underlying circulation, is less well organized during the day, as noted by Cantor et al. (2002) and Sánchez-Lavega et al. (2018). This may be a consequence of day-night differences in the vertical structure and static stability of the lower atmosphere. At night, a temperature inversion forms in the lowest kilometer above the surface (Figs. 1, 7, and 12); this shallow nighttime boundary layer is stably stratified so that vertical mixing is strongly inhibited and the winds above it are decoupled from surface friction. As the surface

warms during the day, the nighttime inversion is replaced by a well-mixed daytime convective boundary layer that extends to the ground (Read et al., 2017), and surface friction increases accordingly. Hence, the wind field at cloud level may vary significantly with time of day, spinning down during the day in response to surface friction and spinning up again at night toward geostrophic balance.

A. Supplementary data

Two supplementary data products are available. The first is an ascii text file that contains information about NMLs and temperature inversions observed in MY27 ("NML_properties_MY27.csv"). The second is a 5-sol animation constructed from MOC WA images of the annular cloud ("Annular_Cloud_MY27.MP4"). Further information about both data products can be found in "Guide_to_Supplementary_Data.pdf".

Acknowledgments. Funding for this research comes from the NASA Mars Data Analysis Program through grants 80NSSC19K0015 (D. Hinson and J. Wilson) and 80NSSC17K0475 (H. Wang). A. Spiga is supported by CNES.

References

Allison, M., 1997. Accurate analytic representations of solar time and seasons on Mars with applications to the Pathfinder/Surveyor missions. Geophysical Research Letters 24, 1967–1970. doi:10.1029/97GL01950.

Allison, M., McEwen, M., 2000. A post-Pathfinder evaluation of areocentric solar coordinates with improved timing recipes for Mars seasonal/diurnal climate studies. Planetary and Space Science 48, 215–235. doi:10.1016/S0032-0633(99)00092-6.

Cantor, B., Malin, M., Edgett, K.S., 2002. Multiyear Mars Orbiter Camera (MOC) observations of repeated Martian weather phenomena during the northern summer season. Journal of Geophysical Research (Planets) 107, 5014. doi:10.1029/2001JE001588.

Clancy, R.T., Sandor, B.J., Wolff, M.J., Christensen, P.R., Smith, M.D., Pearl, J.C., Conrath, B.J., Wilson, R.J., 2000. An intercomparison of ground-based millimeter, MGS TES, and Viking atmospheric temperature measurements: Seasonal and interannual variability of temperatures and dust loading in the global Mars atmosphere. Journal of Geophysical Research (Planets) 105(E4), 9553–9572. doi:10.1029/1999JE001089.

Colaprete, A., Toon, O.B., 2000. The radiative effects of Martian water Ice clouds on the local atmospheric temperature profile. Icarus 145, 524–532. doi:10.1006/icar.2000.6364.

Dickinson, C., Whiteway, J.A., Komguem, L., Moores, J.E., Lemmon, M.T., 2010. Lidar measurements of clouds in the planetary boundary layer on Mars. Geophysical Research Letters 37, L18203. doi:10.1029/2010GL044317.

Gill, A.E., 1982. Atmosphere-Ocean Dynamics. Academic Press, San Diego.

Haberle, R.M., Joshi, M.M., Murphy, J.R., Barnes, J.R., Schofield, J.T., Wilson, G., Lopez-Valverde, M., Hollingsworth, J.L., Bridger, A.F.C., Schaeffer, J., 1999. General circulation model simulations of the Mars Pathfinder atmospheric structure investigation/meteorology data. Journal of Geophysical Research 104, 8957–8974. doi:10.1029/1998JE900040.

Hinson, D., Asmar, S., Kahan, D., Akopian, V., Haberle, R., Spiga, A., Schofield, T., Kleinböhl, A., Abdou, W., Lewis, S., Paik, M., Maalouf, S., 2014. Initial results from radio occultation measurements with the Mars Reconnaissance Orbiter: A nocturnal mixed layer in the tropics and comparisons with polar profiles from the Mars Climate Sounder. Icarus 243, 91–103. doi:10.1016/j.icarus.2014.09.019.

Hinson, D., Simpson, R., Twicken, J., Tyler, L., Flasar, M., 1999. Initial results from radio occultation measurements with Mars Global Surveyor. Journal of Geophysical Research 104, 26997–27012. doi:10.1029/1999JE001069.

Hinson, D., Tyler, D., Lewis, S., Pätzold, M., Tellmann, S., Häusler, B., Tyler, L., 2019. The Martian daytime convective boundary layer: Results from radio occultation measurements and a mesoscale model. Icarus 326, 105–122. doi:10.1016/j.icarus.2019.02.028.

Hinson, D., Wilson, J., 2004. Temperature inversions, thermal tides, and water ice clouds in the Martian tropics. Journal of Geophysical Research (Planets) 109, E01002. doi:10.1029/2003JE002129.

Hinson, D., Wilson, J., Spiga, A., Kahre, M., Hollingsworth, J., 2018. Nocturnal mixed layers and water ice clouds on Mars. AGU Fall Meeting Abstracts P43K-3891. URL: https://doi.org/10.1002%2Fessoar.10500236.1, doi:10.1002/essoar.10500236.1.

Karayel, E.T., Hinson, D.P., 1997. Sub-Fresnel-scale vertical resolution in atmospheric profiles from radio occultation. Radio Science 32, 411–424. doi:10.1029/96RS03212.

Kleinböhl, A., Schofield, J.T., Abdou, W.A., Irwin, P.G.J., de Kok, R.J., 2011. A single-scattering approximation for infrared radiative transfer in limb geometry in the Martian atmosphere. Journal of Quantitative Spectroscopy & Radiative Transfer 112, 1568–1580. doi:10.1016/j.jqsrt.2011.03.006.

Kleinböhl, A., Schofield, J.T., Kass, D.M., Abdou, W.A., Backus, C.R., Sen, B., Shirley, J.H., Lawson, W.G., Richardson, M.I., Taylor, F.W., Teanby, N.A., McCleese, D.J., 2009. Mars Climate Sounder limb profile retrieval of atmospheric temperature, pressure, and dust and water ice opacity. Journal of Geophysical Research (Planets) 114(E10), E10006. doi:10.1029/2009JE003358.

Lemoine, F.G., Smith, D.E., Rowlands, D.D., Zuber, M.T., Neumann, G.A., Chinn, D.S., Pavlis, D.E., 2001. An improved solution of the gravity field of Mars (GMM-2B) from Mars Global Surveyor. Journal of Geophysical Research 106, 23359–23376. doi:10.1029/2000JE001426.

Liu, J., Richardson, M.I., Wilson, R.J., 2003. An assessment of the global, seasonal, and interannual spacecraft record of Martian climate in the thermal infrared. Journal of Geophysical Research (Planets) 108, 5089. doi:10.1029/2002JE001921.

Madeleine, J.B., Forget, F., Millour, E., Navarro, T., Spiga, A., 2012. The influence of radiatively active water ice clouds on the Martian climate. Geophysical Research Letters 39, L23202. doi:10.1029/2012GL053564.

Malin, M.C., Edgett, K.S., 2001. Mars Global Surveyor Mars Orbiter Camera: Interplanetary cruise through primary mission. Journal of Geophysical Research 106, 23429–23570. doi:10.1029/2000JE001455.

Malin, M.C., Edgett, K.S., Cantor, B.A., Caplinger, M.A., Danielson, G.E., Jensen, E.H., Ravine, M.A., Sandoval, J.L., Supulver, K.D., 2010. An overview of the 1985-2006 Mars Orbiter Camera science investigation. International Journal of Mars Science and Exploration 4, 1–60. doi:10.1555/mars.2010.0001.

McCleese, D.J., Heavens, N.G., Schofield, J.T., Abdou, W.A., Bandfield, J.L., Calcutt, S.B., Irwin, P.G.J., Kass, D.M., Kleinböhl, A., Lewis, S.R., Paige, D.A., Read, P.L., Richardson, M.I., Shirley, J.H., Taylor, F.W., Teanby, N., Zurek, R.W., 2010. Structure and dynamics of the Martian lower and middle atmosphere as observed by the Mars Climate Sounder: Seasonal variations in zonal mean temperature, dust, and water ice aerosols. Journal of Geophysical Research (Planets) 115, E12016. doi:10.1029/2010JE003677.

McCleese, D.J., Schofield, J.T., Taylor, F.W., Calcutt, S.B., Foote, M.C., Kass, D.M., Leovy, C.B., Paige, D.A., Read, P.L., Zurek, R.W., 2007. Mars Climate Sounder: An investigation of thermal and water vapor structure, dust and condensate distributions in the atmosphere, and energy balance of the polar regions. Journal of Geophysical Research (Planets) 112, E05S06. doi:10.1029/2006JE002790.

Owen, T., 1992. The composition and early history of the atmosphere of Mars. In: Kieffer, H. H., Jakosky, B. M., Snyder, C. W., Matthews, M. S. (Eds.), Mars. Univ. of Arizona Press, Tucson. pp. 818–834.

Pankine, A.A., Tamppari, L.K., 2015. Constraints on water vapor vertical distribution at the Phoenix landing site during summer from MGS TES day and night observations. Icarus 252, 107–120. doi:10.1016/j.icarus.2015.01.008.

Read, P.L., Galperin, B., Larsen, S.E., Lewis, S.R., Määttänen, A., Petrosyan, A., Rennó, N., Savijärvi, H., Siili, T., Spiga, A., Toigo, A., Vázquez, L., 2017. The Martian Planetary Boundary Layer. In: In: Haberle, R. M., Clancy, R. T., Forget, F., Smith, M. D., Zurek, R. W. (Eds.), The Atmosphere and Climate of Mars. Cambridge University Press. pp. 172–202. doi:10.1017/9781139060172.007.

Sánchez-Lavega, A., Garro, A., del Río-Gaztelurrutia, T., Hueso, R., Ordoñez-Etxeberria, I., Chen Chen, H., Cardesín-Moinelo, A., Titov, D., Wood, S., Almeida, M., Spiga, A., Forget, F., Määttänen, A., Hoffmann, H., Gondet, B., 2018. A Seasonally recurrent annular cyclone in Mars northern latitudes and observations of a companion vortex. Journal of Geophysical Research (Planets) 123, 3020–3034. doi:10.1029/2018JE005740.

Smith, M.D., 2004. Interannual variability in TES atmospheric observations of Mars during 1999-2003. Icarus 167, 148–165. doi:10.1016/j.icarus.2003.09.010.

Spiga, A., Forget, F., Lewis, S., Hinson, D., 2010a. Structure and dynamics of the convective boundary layer on Mars as inferred from large-eddy simulations and remote-sensing measurements. Quarterly Journal of the Royal Meteorological Society 136, 414–428. doi:10.1002/qj.563.

Spiga, A., Forget, F., Lewis, S., Hinson, D., 2010b. Correction to: 'Structure and dynamics of the convective boundary layer on Mars as inferred from large-eddy simulations and remote-sensing measurements'. Quarterly Journal of the Royal Meteorological Society 136, 2205–2206. doi:10.1002/qj.725.

Spiga, A., Hinson, D.P., Madeleine, J.B., Navarro, T., Millour, E., Forget, F., Montmessin, F., 2017. Snow precipitation on Mars driven by cloud-induced night-time convection. Nature Geoscience 10, 652–657. doi:10.1038/ngeo3008.

Thayer, G.D., 1974. An improved equation for the radio refractive index of air. Radio Science 9, 803–807. doi:10.1029/RS009i010p00803.

Tyler, D., Barnes, J.R., 2014. Atmospheric mesoscale modeling of water and clouds during northern summer on Mars. Icarus 237, 388–414. doi:10.1016/j.icarus.2014.04.020.

Wang, H., 2016. MGS MOC Mars Daily Global Maps. URL: https://doi.org/10.7910/DVN/WWRT1V, doi:10.7910/DVN/WWRT1V.

Wang, H., Fisher, J.A., 2009. North polar frontal clouds and dust storms on Mars during spring and summer. Icarus 204, 103–113. doi:10.1016/j.icarus.2009.05.028.

Wang, H., Ingersoll, A.P., 2002. Martian clouds observed by Mars Global Surveyor Mars Orbiter Camera. Journal of Geophysical Research (Planets) 107, 5078. doi:10.1029/2001JE001815.

Whiteway, J.A., Komguem, L., Dickinson, C., Cook, C., Illnicki, M., Seabrook, J., Popovici, V., Duck, T.J., Davy, R., Taylor, P.A., Pathak, J., Fisher, D., Carswell, A.I., Daly, M., Hipkin, V., Zent, A.P., Hecht, M.H., Wood, S.E., Tamppari, L.K., Renno, N., Moores, J.E., Lemmon, M.T., Daerden, F., Smith, P.H., 2009. Mars water-Ice clouds and precipitation. Science 325, 68–70. doi:10.1126/science.1172344.

Wilson, R.J., Guzewich, S.D., 2014. Influence of water ice clouds on nighttime tropical temperature structure as seen by the Mars Climate Sounder. Geophysical Research Letters 41, 3375–3381. doi:10.1002/2014GL060086.

Wilson, R.J., Lewis, S.R., Montabone, L., Smith, M.D., 2008. Influence of water ice clouds on Martian tropical atmospheric temperatures. Geophysical Research Letters 35, L07202. doi:10.1029/2007GL032405.

Wilson, R.J., Neumann, G.A., Smith, M.D., 2007. Diurnal variation and radiative influence of Martian water ice clouds. Geophysical Research Letters 34, L02710. doi:10.1029/2006GL027976.